

**Two-Dimensional Depth-Averaged Flow Modeling
with an Unstructured Hybrid Mesh**

by

Yong G. Lai¹

ABSTRACT

An unstructured hybrid mesh numerical method is developed to simulate open channel flows. The method is applicable to arbitrarily-shaped mesh cells and offers a framework to unify many mesh topologies into a single formulation. The finite-volume discretization is applied to the two-dimensional depth-averaged St. Venant equations, and the mass conservation is satisfied both locally and globally. An automatic wetting-drying procedure is incorporated in conjunction with the segregated solution procedure that chooses the water surface elevation as the main variable. The method is applicable to both steady and unsteady flows and covers the entire flow range: subcritical, transcritical and supercritical. The proposed numerical method is well suited to natural river flows with a combination of main channels, side channels, bars, floodplains and in-stream structures. Technical details of the method are presented, verification studies are performed using a number of simple flows, and a practical natural river is modeled to illustrate issues of calibration and validation.

KEYWORDS: 2D Model, Depth-Averaged Model, Hybrid Mesh, Unstructured Mesh

¹Hydraulic Engineer, Sedimentation and River Hydraulics Group, Technical Service Center, Bureau of Reclamation, Denver, CO 80225; PH: 303-445-2560; FAX: 303-445-6351; email: ylai@do.usbr.gov

1. INTRODUCTION

One-dimensional (1D) flow models have been routinely used in practical hydraulic applications. Example models include HEC-RAS (Brunner, 2006), MIKE11 (DHI, 2002), CCHE1D (Wu and Vieira, 2002), and SRH-1D (Huang and Greimann, 2007). These 1D models will remain useful, particularly for applications with a long river reach (e.g., more than 50 km) or over a long time period (e.g., over a year). Their limitations, however, are well known and there are situations where multi-dimensional modeling is needed. For most river flows, water depth is shallow relative to width and vertical acceleration is negligible in comparison with gravity. So the two-dimensional (2D) depth-averaged model provides the next level of modeling accuracy for many practical open channel flows. Indeed, time has been ripe that 2D models may be routinely used for river projects on a personal computer.

A range of 2D models have been developed and applied to a wide range of problems since the work of Chow and Ben-Zvi (1973). Examples include Harrington et al. (1978), McGuirk and Rodi (1978), Vreugdenhil and Wijnbenga (1982), Jin and Steffler (1993), Ye and McCorquodale (1997), Ghamry and Steffler (2005), Zarrati et al. (2005), Begnudelli and Sanders (2006), among many others. Examples of commercial or public-domain 2D codes include MIKE 21 (DHI, 1996), RMA2 (USACE, 1996), CCHE2D (Jia and Wang, 2001), TELEMAC (Hervouet and van Haren, 1996), etc.

The ability of a 2D model to solve open channel flows with complex geometries has always been a thrust for improvement as it is relevant to practical applications. One of the recent advances is the use of hierarchical mesh approaches using the adaptive meshing as reported by Kramer and Jozsa (2007). An alternative approach of adopting hybrid meshes is pursued in this study. At present, non-orthogonal structured meshes with a curvilinear

coordinate system have been widely used within the finite difference and finite volume framework, while unstructured meshes with fixed cell shapes, quadrilaterals or triangles, have been used with the finite element method. Meshing method based on a fixed cell shape may be appropriate for one application but problematic for another. In general, near-orthogonal quadrilateral cells give good solutions with added benefit of allowing mesh stretching along the river main channel. Such cells, however, are very restrictive in representing a natural river which typically includes different features such as main channels, side channels, and floodplains. Triangular cells are easy to generate and the method alleviates the rigidity of the structured mesh in that it allows flexible mesh point clustering. Unfortunately, stretched triangles are inefficient and less accurate (e.g., Baker, 1996; Lai et al., 2003). The best compromise, therefore, is to use a hybrid mesh in which a combination of quadrilaterals and triangles is used. The author's experience (Lai, 2006) showed that a good meshing strategy, in terms of efficiency and accuracy, is to represent the main channel and important areas with quadrilaterals and the rest of areas with triangles. Specifically, quadrilateral cells may be used in the main channel and be stretched along the flow direction, while triangular cells may be used to fill the floodplains and bars with mesh density control. The advantage of a hybrid mesh was recognized by Bernard and Berger (1999) who proposed the coupling of two flow codes: one with a structured quadrilateral mesh and another with an unstructured triangular mesh.

In this paper, an unstructured hybrid mesh numerical method is developed to simulate open channel flows, following the three-dimensional work of Lai (2003). The proposed methodology is applicable to arbitrarily shaped mesh cells, and not limited to quadrilaterals or triangles. The advantage of the arbitrarily shaped cell method is that the same numerical solver is used with most mesh topologies in use. For example, the method may be used

with: the orthogonal or non-orthogonal structured quadrilateral mesh, the unstructured triangular mesh, the hybrid mesh with mixed cell shapes, and the Cartesian mesh with stair cases.

In the following, the numerical formulation applicable to arbitrarily shaped cells is presented first for the 2D depth averaged equations. The method is implemented into a numerical model that is applied to a number of open channel flows for the purpose of testing and verification. Further validation and demonstration of the model are achieved by applying the model to a practical natural river flow. An extensive list of applications have been carried out with the proposed numerical model; they may be found in Lai (2006) and the associated website. The model is also downloadable from the website.

2. NUMERICAL METHOD

2.1 Governing Equations

Most open channel flows are relatively shallow and the effect of vertical motions is negligible. As a result, the three-dimensional Navier-Stokes equations may be vertically averaged to obtain a set of depth-averaged 2D equations, leading to the following standard St. Venant equations:

$$\frac{\partial h}{\partial t} + \frac{\partial hU}{\partial x} + \frac{\partial hV}{\partial y} = 0 \quad (1)$$

$$\frac{\partial hU}{\partial t} + \frac{\partial hUU}{\partial x} + \frac{\partial hVU}{\partial y} = \frac{\partial hT_{xx}}{\partial x} + \frac{\partial hT_{xy}}{\partial y} - gh \frac{\partial z}{\partial x} - \frac{\tau_{bx}}{\rho} \quad (2)$$

$$\frac{\partial hV}{\partial t} + \frac{\partial hUV}{\partial x} + \frac{\partial hVV}{\partial y} = \frac{\partial hT_{xy}}{\partial x} + \frac{\partial hT_{yy}}{\partial y} - gh \frac{\partial z}{\partial y} - \frac{\tau_{by}}{\rho} \quad (3)$$

In the above, x and y are horizontal Cartesian coordinates, t is time, h is still water depth, U and V are depth-averaged velocity components in x and y directions, respectively, g is gravitational acceleration, T_{xx} , T_{xy} , and T_{yy} are depth-averaged stresses due to turbulence as well as dispersion, $z = z_b + h$ is water surface elevation, z_b is bed elevation, ρ is water density, and τ_{bx}, τ_{by} are bed shear stresses. The bed stresses are obtained using the Manning's resistance equation as:

$$(\tau_{bx}, \tau_{by}) = \rho U_*^2 \frac{(U, V)}{\sqrt{U^2 + V^2}} = \rho C_f \sqrt{U^2 + V^2} (U, V) \quad (4)$$

where $C_f = \frac{gn^2}{h^{1/3}}$, n is Manning's roughness coefficient, and U_* is bed frictional velocity.

Effective stresses are calculated with the Boussinesq's formulation as:

$$\begin{aligned} T_{xx} &= 2(\nu + \nu_t) \frac{\partial U}{\partial x} - \frac{2}{3} k; & T_{xy} &= (\nu + \nu_t) \left(\frac{\partial U}{\partial y} + \frac{\partial V}{\partial x} \right) \\ T_{yy} &= 2(\nu + \nu_t) \frac{\partial V}{\partial y} - \frac{2}{3} k \end{aligned} \quad (5)$$

where ν is kinematic viscosity of water, ν_t is eddy viscosity, and k is turbulent kinetic energy.

The eddy viscosity is calculated with a turbulence model. Two models are used in this study (Rodi, 1993): the depth-averaged parabolic model and the two-equation $k-\varepsilon$ model. For the parabolic model, the eddy viscosity is calculated as $\nu_t = C_t U_* h$ and the frictional velocity U_* is defined in (4). The model constant C_t may range from 0.3 to 1.0; a default value of $C_t = 0.7$ is used in this study. For the two-equation $k-\varepsilon$ model, the eddy viscosity is calculated as $\nu_t = C_\mu k^2 / \varepsilon$ with the two additional equations as follows:

$$\frac{\partial hk}{\partial t} + \frac{\partial hUk}{\partial x} + \frac{\partial hVk}{\partial y} = \frac{\partial}{\partial x} \left(\frac{h\nu_t}{\sigma_k} \frac{\partial k}{\partial x} \right) + \frac{\partial}{\partial y} \left(\frac{h\nu_t}{\sigma_k} \frac{\partial k}{\partial y} \right) + P_h + P_{kb} - h\varepsilon \quad (6)$$

$$\frac{\partial h\varepsilon}{\partial t} + \frac{\partial hU\varepsilon}{\partial x} + \frac{\partial hV\varepsilon}{\partial y} = \frac{\partial}{\partial x} \left(\frac{h\nu_t}{\sigma_\varepsilon} \frac{\partial \varepsilon}{\partial x} \right) + \frac{\partial}{\partial y} \left(\frac{h\nu_t}{\sigma_\varepsilon} \frac{\partial \varepsilon}{\partial y} \right) + C_{\varepsilon 1} \frac{\varepsilon}{k} P_h + P_{\varepsilon b} - C_{\varepsilon 2} h \frac{\varepsilon^2}{k} \quad (7)$$

The expressions of some terms, along with the model coefficients, follow the recommendation of Rodi (1993); they are listed below:

$$P_h = h\nu_t \left[2 \left(\frac{\partial U}{\partial x} \right)^2 + 2 \left(\frac{\partial V}{\partial y} \right)^2 + \left(\frac{\partial U}{\partial y} + \frac{\partial V}{\partial x} \right)^2 \right] \quad (8)$$

$$P_{kb} = C_f^{-1/2} U_*^3; \quad P_{\varepsilon b} = C_{\varepsilon f} C_{\varepsilon 2} C_\mu^{1/2} C_f^{-3/4} U_*^4 / h \quad (9)$$

$$C_\mu = 0.09, C_{\varepsilon 1} = 1.44, C_{\varepsilon 2} = 1.92, \sigma_k = 1, \sigma_\varepsilon = 1.3, C_{\varepsilon f} = 1.8 \sim 3.6 \quad (10)$$

The terms P_{kb} and $P_{\varepsilon b}$ are added to account for the generation of turbulence energy and dissipation due to bed friction in case of uniform flows.

2.2 Boundary Conditions

Boundary conditions consist of four types: inlet, exit, solid wall, and symmetry. An inlet is defined as a boundary segment on the solution domain where flow is to move into the domain. At an inlet, a total flow discharge, in the form of a constant or a time series hydrograph, is specified. Velocity distribution along the inlet is calculated in a way that the total discharge is satisfied. If a flow is subcritical at an inlet, the water surface elevation is not needed and is calculated assuming that the water surface slope normal to the inlet is constant. If a flow is supercritical at an inlet, the water surface elevation at the inlet is needed as another boundary condition. If the k - ε turbulence model is used, k and ε values are also needed which, for most applications, have negligible impact on the flow pattern (Rodi, 1993).

An exit is defined as a boundary segment on the solution domain where flow is to move out of the domain. At a subcritical exit, only the water surface elevation is needed as the boundary condition. No boundary condition is needed if a flow at an exit is supercritical. Variables at an exit are extrapolated from the adjacent cells by assuming that the derivatives of variables normal to the boundary are constant.

At a solid wall, no-slip condition is applied and the wall functions are employed. The flow shear stress vector at a solid wall is calculated by $(\tau_{wx}, \tau_{wy}) = \rho C_\mu^{1/4} k_P^{1/2} \frac{\kappa(U, V)}{\ln(Ey_P^+)}$ with

$$y_P^+ = C_\mu^{1/4} k_P^{1/2} y_P / \nu \text{ for the } k - \varepsilon \text{ model; and } (\tau_{wx}, \tau_{wy}) = \rho U_* \frac{\kappa(U, V)}{\ln(Ey_P^+)}$$

with $y_P^+ = U_* y_P / \nu$ for the depth-averaged parabolic model. In the above, k_P is turbulent kinetic energy at a mesh cell that contains the wall boundary, $\kappa = 0.41$ is the von Kármán constant, y_P is normal distance from the center of a cell to a wall, and E is a constant.

Symmetry is a boundary where all dependent variables are extrapolated assuming the gradient of a variable in a direction normal to the boundary is zero except for the normal velocity component (normal to the boundary). The normal velocity component is set to zero at a symmetry boundary.

2.3 Discretization

The 2D depth-averaged equations (1) to (3) may be written in tensor form as:

$$\frac{\partial h}{\partial t} + \nabla \cdot (h\vec{V}) = 0 \quad (11)$$

$$\frac{\partial (h\vec{V})}{\partial t} + \nabla \cdot (h\vec{V}\vec{V}) = -gh\nabla z + \nabla \cdot \left(h\vec{T} \right) - \frac{\vec{\tau}_b}{\rho} \quad (12)$$

where \vec{V} is the velocity vector, \vec{T} is the 2nd-order stress tensor, with its component defined in (5), and $\vec{\tau}_b$ is the bed shear stress vector. The governing equations are discretized using the segregated finite-volume approach of Lai et al. (2003). The solution domain is covered with an unstructured mesh and cells may assume the shapes of arbitrary polygons. All dependent variables are stored at the geometric centers of the polygonal cells. The governing equations are integrated over polygonal cells using the Gauss integral. As an illustration, consider a generic convection-diffusion equation that is representative of all governing equations:

$$\frac{\partial h\Phi}{\partial t} + \nabla \bullet (h\vec{V}\Phi) = \nabla \bullet (\Gamma\nabla\Phi) + S_\Phi^* \quad (13)$$

Here Φ denotes a dependent variable, a scalar or a component of a vector, Γ is diffusivity coefficient, and S_Φ^* is the source/sink term. Integration over an arbitrarily shaped polygon P shown in Fig. 1 leads to:

$$\frac{(h_P^{n+1}\Phi_P^{n+1} - h_P^n\Phi_P^n)A}{\Delta t} + \sum_{all-sides} (h_C V_C |\vec{s}|)^{n+1} \Phi_C^{n+1} = \sum_{all-sides} (\Gamma_C^{n+1} \nabla\Phi^{n+1} \bullet \vec{n} |\vec{s}|) + S_\Phi \quad (14)$$

In the above, Δt is time step, A is cell area, $V_C = \vec{V}_C \bullet \vec{n}$ is velocity component normal to the polygonal side (e.g., P_1P_2 in Fig.1) and is evaluated at the side center C , \vec{n} is unit normal vector of a polygon side, \vec{s} is the polygon side distance vector (e.g., from P_1 to P_2 in Fig.1), and $S_\Phi = S_\Phi^* A$. Subscript C indicates a value evaluated at the center of a polygon side and superscript, n or $n+1$, denotes the time level. In the remaining discussion, superscript $n+1$ will be dropped for ease of notation. Note that the Euler implicit time discretization is adopted. The remaining task is to obtain appropriate expressions for the convective and diffusive fluxes at each polygon side.

Discretization of the diffusion term, the first on the right hand side of (14), is carried out first and the final expression is derived as:

$$\nabla\Phi \cdot \vec{n} |\vec{s}| = D_n (\Phi_N - \Phi_P) + D_c (\Phi_{P_2} - \Phi_{P_1}) \quad (15)$$

$$D_n = \frac{|\vec{s}|}{(\vec{r}_1 + \vec{r}_2) \cdot \vec{n}}; \quad D_c = -\frac{(\vec{r}_1 + \vec{r}_2) \cdot \vec{s} / |\vec{s}|}{(\vec{r}_1 + \vec{r}_2) \cdot \vec{n}} \quad (16)$$

In the above, \vec{r}_1 is the distance vector from P to C and \vec{r}_2 is from C to N . The “normal” and “cross” diffusion coefficients, D_n and D_c , at each polygon side involve only geometric variables; they are calculated only once in the beginning of the computation.

Computation of a variable, say Y , at the center C of a polygon side is discussed next. This is an interpolation operation used frequently. A second-order accurate expression is derived next. As shown in Figure 1, the point I is defined as the intercept point between line PN and line P_1P_2 . A second-order interpolation for point I may be expressed as

$$Y_I = \frac{\delta_1 Y_N + \delta_2 Y_P}{\delta_1 + \delta_2} \quad (17)$$

in which $\delta_1 = \vec{r}_1 \cdot \vec{n}$ and $\delta_2 = \vec{r}_2 \cdot \vec{n}$. Y_I may be used to approximate the value at the side center C . This treatment, however, does not guarantee second-order accuracy unless \vec{r}_1 and \vec{r}_2 are parallel. A truly second-order expression is derived as:

$$Y_C = Y_I - C_{side} (Y_{P_2} - Y_{P_1}) \quad (18)$$

$$C_{side} = \frac{(\delta_1 \vec{r}_2 - \delta_2 \vec{r}_1) \cdot \vec{s}}{(\delta_1 + \delta_2) |\vec{s}|^2} \quad (19)$$

The extra term in the above is similar in form to the cross diffusion term in (16).

Φ_C in the convective term of (14) needs further discussion. If the second-order central scheme is used directly, spurious oscillations may occur for flows with a high cell Peclet

number (Patankar, 1980). Therefore, a damping term is added to the central difference scheme similar to the concept of artificial viscosity. The damped scheme is as follows:

$$\Phi_C = \Phi_C^{CN} + d(\Phi_C^{UP} - \Phi_C^{CN}) \quad (20)$$

$$\Phi_C^{UP} = \frac{1}{2}(\Phi_P + \Phi_N) + \frac{1}{2} \text{sign}(V_C)(\Phi_P - \Phi_N) \quad (21)$$

where Φ_C^{CN} stands for the second-order scheme expressed in (18). In the above, d defines the amount of damping and $d = 0.2 \sim 0.3$ is usually used. Note that d is not a calibration parameter and it affects only the accuracy slightly. A fixed value of 0.3 is used for all cases presented.

The final discretized equation at mesh cell P may be organized as a linear equation:

$$A_P \Phi_P = \sum_{nb} A_{nb} \Phi_{nb} + S_{diff} + S_{conv} + S_\Phi \quad (22)$$

where “ nb ” refers to all neighbor cells surrounding cell P . The coefficients in (22) are:

$$A_{nb} = \Gamma_C D_n + \text{Max}(0, -h_C V_C |\vec{s}|) \quad (23a)$$

$$A_P = \frac{h_P^n A}{\Delta t} + \sum_{nb} A_{nb} \quad (23b)$$

$$S_{diff} = \frac{h_P^n A}{\Delta t} + \sum_{all\ sides} \Gamma_C D_c (\Phi_{P2} - \Phi_{P1}) \quad (23c)$$

$$S_{conv} = \sum_{all\ sides} (h_C V_C |\vec{s}|) \left\{ (1-d) \left[\frac{\delta_1}{\delta_1 + \delta_2} - \frac{1 - \text{sign}(V_C)}{2} \right] (\Phi_N - \Phi_P) \right\} \\ - \sum_{all\ sides} (h_C V_C |\vec{s}|) [(1-d) C_{side} (\Phi_{P2} - \Phi_{P1})] \quad (23d)$$

2.4 Side Normal Velocity and Elevation Correction Equation

For a non-staggered mesh, a special procedure is used to obtain the polygon side normal velocity that is used to enforce the mass conservation. Otherwise the well-known

checkerboard instability may appear (Rhie and Chow, 1983). Here the procedure proposed by Rhie and Chow (1983) and Peric et al. (1988) is adopted. That is, the normal velocity is obtained by averaging the momentum equation from cell centers to cell sides. A detailed derivation is omitted, and interested readers are referred to the previous work (e.g., Rhie and Chow, 1983; Peric et al., 1988; and Lai et al. 1995). It is sufficient to present only the final form of the equation as follows:

$$V_C = \langle \vec{V} \rangle \bullet \vec{n} + \left\langle \frac{A}{A_P} \right\rangle \langle gh \nabla z \rangle \bullet \vec{n} - \left\langle \frac{A}{A_P} \right\rangle gh \nabla z \bullet \vec{n} \quad (24)$$

where “ $\langle \rangle$ ” stands for the interpolation operation from mesh cell center to side as expressed in (18). When a vector appears in the interpolation operation, the interpolation is applied to each Cartesian component of the vector.

The velocity-elevation coupling is achieved using a method similar to the SIMPLEC algorithm (Patankar, 1980). In essence, if elevation z^n is known from a previous time step or iteration, an intermediate velocity is obtained first by solving the linearized momentum equation:

$$A_P \vec{V}_P^* = \sum_{nb} A_{nb} \vec{V}_N^* - a \nabla z^n + \vec{S}_V \quad (25)$$

where a is a constant. Next, we seek velocity correction $\vec{V}' = \vec{V}^{n+1} - \vec{V}^*$ and elevation correction $z' = z^{n+1} - z^n$ such that both the momentum and the mass conservation equations are satisfied. For the momentum equation, it is

$$A_P \vec{V}_P^{n+1} = \sum_{nb} A_{nb} \vec{V}_N^{n+1} - a \nabla z^{n+1} + \vec{S}_V \quad (26)$$

Or, the following correction equation is obtained:

$$A_P \vec{V}_P' = \sum_{nb} A_{nb} \vec{V}_N' - a \nabla z' \quad (27)$$

With the SIMPLEC algorithm, the above may be approximated as:

$$\vec{V}_P' = - \frac{a}{A_P - \sum_{nb} A_{nb}} \nabla z' \quad (28)$$

Substitution of the above into the mass conservation equation leads to the following elevation correction equation:

$$\frac{z'}{\Delta t} + \nabla \cdot (\vec{V} z') = \nabla \cdot \left(\frac{ah}{A_P - \sum_{nb} A_{nb}} \nabla z' \right) - \nabla \cdot (h^n \vec{V}^*) \quad (29)$$

The above elevation correction equation is solved for z' , and (28) is then used to obtain the velocity correction. A number of iterations are usually needed within each time step if the flow is unsteady; but only one iteration is used for a steady state simulation.

Governing equations are solved in a segregated manner. In a typical iterative solution process, momentum equations are solved first assuming known water surface elevation and eddy viscosity at a previous time step. The newly obtained velocity is used to calculate the normal velocity at cell sides using (24). This side velocity will usually not satisfy the continuity equation. Therefore, the elevation correction equation (29) is solved to obtain a new elevation, and subsequently a new velocity with (28). Other scalar equations, such as turbulence, are solved after the elevation correction equation. This completes one iteration of the solution cycle. The above iterative process may be repeated within one time step until a preset residual criterion for each equation is met. The solution would then advance to the next time step. In this study, the residual of a governing equation is defined as the sum of absolute residuals at all mesh cells. The implicit solver requires the solution of non-symmetric sparse matrix linear equations (25) and (29). In this study, the standard conjugate gradient solver with ILU preconditioning is used (Lai, 2000).

2.5 Wetting-Drying Treatment

Most natural rivers consist of main and side channels, bars, islands, and floodplains and bed may be wet or dry depending on flow stage. The wetting-drying property is not known and is part of the solution. A robust wetting-drying algorithm, therefore, is needed. Such an algorithm offers the benefit that the same solution domain and mesh may be used for all flow discharges, eliminating the need to generate multiple meshes.

The wetting-drying algorithm of this study consists of a number of operations. The “cell-coloring” operation identifies mesh cells as either wet or dry. A cell is wet if water depth is above 1.0 mm. Solutions are computed only in wet cells. After new solutions, the “edge-searching” operation is carried out to identify all mesh sides which have one of the neighboring cells wet and the other dry. Finally, the “re-wetting” operation is performed to check whether an edge is to be re-wetted. If water surface elevation of the wet cell is higher than bed elevation of the dry cell, the edge and the associated dry cell are set up as wet for the next time step. The above wetting-drying algorithm is repeated for each time step and it works well with the present numerical method. Both mass and momentum are conserved by the procedure as there is no artificial water redistribution.

3. MODEL TESTING AND VERIFICATION

The hybrid numerical method is implemented into a code named SRH-2D, and a number of simple open channel flows are simulated next for testing and verification.

3.1. Subcritical Flow in a 1D Channel

MacDonald (1996) presented a number of non-trivial analytical test cases for 1D steady St. Venant equations. Test Case 1 is selected here which has a horizontal extent of 1000m by 10m, and a variable bed slope. The flow discharge is $15 \text{ m}^3/\text{s}$, the water depth at

the exit is 0.7484m, the Manning's roughness coefficient is 0.03, and the Froude number of the flow ranges from 0.40 to 0.77. A quadrilateral mesh with 80-by-3 cells is used. Simulated water surface elevation is compared with the analytical solutions of MacDonald (1996) in Figure 2. It is seen that the simulated results match well with those of the analytical solution.

3.2 Transcritical Flow in a 1D Channel

Test Case 6 of MacDonald (1996) is selected next. The case has a transition from subcritical to supercritical flow and a hydraulic jump is formed. The horizontal extent of the simulation is 150m by 10m with a variable bed slope. The flow discharge is $20 \text{ m}^3/\text{s}$, the water depth at the exit is 1.7m, and the Manning's roughness coefficient is 0.031752. A quadrilateral mesh with 120-by-3 cells is used. Simulated profile of water surface elevation is compared with the analytical solution in Figure 3. It is seen that a hydraulic jump is formed while the upstream subcritical flow transitions quickly to supercritical. Comparison is good along with the capturing of the hydraulic jump.

3.3. 2D Diversion Flow

Bifurcation often occurs in open channel flows, and flow features are complex in the diversion area. A particular diversion flow case, measured and studied by Shetta and Murthy (1996), is simulated. The solution domain consists of a main channel, 6.0m in length (X direction) and 0.3m in width (Y direction), and a side channel normal to the main channel at $X=3.0\text{m}$. The side channel has a length of 3.0m and width of 0.3m. The layout of the solution domain, along with the simulated flow pattern, is shown in Figure 4. A structured quadrilateral mesh is generated. The mesh for the main channel has 120-by-30 cells, while the side channel has 40-by-30 cells. The flow discharge in the main channel is $0.00567 \text{ m}^3/\text{s}$; the water elevation at the exit of the main channel ($X=6.0\text{m}$) is 0.0555m; the

water elevation at the exit of the side channel ($Y=3.3\text{m}$) is 0.0465m ; and the Manning's roughness coefficient is 0.012 . Both the parabolic turbulence model and the $k - \varepsilon$ model are used.

Model results are compared with the measured data of Shettar and Murthy (1996). Figure 5 is the water surface elevation along both walls of the main and side channels and Figures 6 and 7 are the depth averaged velocity profiles in both channels. The simulated flow pattern is shown in Figure 4. It is seen that the water elevation in the main channel is predicted well by both turbulence models but discrepancy is noticeable in the side channel for the parabolic model. The velocity profiles and the related flow recirculation are also reasonably predicted. The predicted flow separations at the entrance of the side channel and near the bottom of the main channels agree well with the experimental visualization of Shettar and Murthy (1996) for the $k - \varepsilon$ model. Larger discrepancies, however, are observed for the parabolic model. For example, the velocity near the bottom wall ($Y=0$) of the main channel is over-predicted. Model runs in this study show that the parabolic model give reasonable results for most portion of the flow but not for the area with flow separation. It is mainly due to the inaccurate near-wall turbulence represented by the parabolic model.

3.4. Meandering Channel with 90° Bends

Meander is a common feature of natural rivers and is therefore an important configuration for simulation. The meandering channel measured and computed by Zarrati et al. (2005) is simulated. The channel consists of 10 sections with a rectangular cross section of 0.3m in width. Each section has a 90° circular bend with the centerline radius of 0.6m , followed by a 0.3m straight channel. The channel slope is $1/1,000$. At a flow discharge of $0.002 \text{ m}^3/\text{s}$, the average flow depth is about 0.03m , the Froude number is 0.42 , and the

estimated Manning's coefficient is 0.013. This case has the width-to-depth ratio of 10 and the radius-to-width ratio of 2.0. Typical width-to-depth ratio of a natural meander is between 7 and 10 or 20 and 50 (Schumm, 1960) and the radius-to-width ratio around 2.3 (Leopold and Wolman, 1960).

The solution domain includes two bend sections as shown in Figure 8. Results from three meshes are presented: a structured mesh with 160-by-20 quadrilateral cells (Fig.8), an unstructured triangular mesh with 3,326 cells (Fig.9a), and a hybrid mesh with 3,190 mixed cells (Fig.9b). Mesh sensitivity study with the structured mesh was carried out and it showed that 160-by-20 cells were sufficient to achieve a mesh independent solution. The $k - \varepsilon$ model was used for comparison.

Model results are compared with the measured data of Zarrati et al. (2005) in Fig.8 at three lateral cross sections: E, F and G. The predicted water depth distribution is shown in Fig.10 and the predicted depth-averaged velocity is in Fig.11. It is found that the water surface elevations predicted by three meshes are almost the same, indicating that elevation prediction is less sensitive to the mesh choice. Mesh sensitivity study results also lead to the same conclusion; water elevation is well predicted even with a very coarse mesh. However, the velocity prediction is more sensitive to the mesh size and type. Results in Fig.11 show that the discrepancy in velocity prediction is mainly near the bank. The structured and hybrid meshes produce very similar results. However, the unstructured triangular mesh is less accurate if similar number of cells is used. It is known that the triangular cells are less accurate and more triangular cells are needed to achieve the same level of accuracy as the quadrilateral cells (Lai et al. 2003). To find out if it is true for the present case, the number of triangular cells is doubled and simulation is carried out again

with the new mesh. It is found that more accurate results are obtained when the number of triangular cells is doubled and the new results are similar to those of the structured mesh.

4. SANDY RIVER DELTA SIMULATION

Sandy River Delta (SRD) dam is located near the confluence of the Sandy and Columbia Rivers, east of Portland, Oregon (Fig.12). As a result of its closure in 1938, flow has been redirected from the east (upstream) distributary to the west (downstream) distributary. Although it was once the main distributary channel, the east distributary is currently only activated under high flow conditions. Recent efforts to improve aquatic habitat conditions have considered the removal of the dam. The 2D model presented in this paper was used to evaluate possible effects on the delta area if the dam is removed. Both hydraulic and sediment studies were carried out; but only the calibration and validation study with the hydraulic flow is presented. More results, as well as the details of the study, may be found in the report by Lai et al. (2006).

4.1 Bathymetry, Solution Domain, and Mesh

Topographical information for the study area was obtained from the cross-sectional survey and the Lidar data in October 2005 (Lai et al., 2006). The bed elevation contours of the study area are displayed in Fig.12. The solution domain consists of 15.3 km of the Columbia River and 4.2 km of the Sandy River with an area of about 33.2 km². The solution domain was covered with a hybrid mesh with a total of 37,637 cells, in which the main channels are quadrilaterals stretched in the flow direction while the remaining areas were covered with a combination of triangular and quadrilateral cells. For viewing clarity, only a portion of the mesh around the delta area is shown in Fig.13. The mesh is fine

enough to represent the model area as a mesh with 50% more cells did not change the water elevation and velocities by more than 3%.

4.2 Model Parameters

Flow resistance is a model input represented by the Manning’s coefficient (n); it is usually the only calibration parameter. A single n -value approach is inappropriate for the case as the solution domain consists of widely different bed types - main channels with different bed gradations, point bars, and vegetated floodplains. Therefore, the solution domain was divided into a number of roughness zones (Fig.14) based on the underlying bed properties, delineated using the available aerial photo and the bed gradation data. In Fig.14, zones 1, 2 and 3 represent the main channel of the Sandy River; zones 4 and 5 represent the main channel of the Columbia River; zone 6 consists mostly of sand bars and less vegetated areas; and zone 7 represents islands and floodplains with heavy vegetation. Each zone was assigned a Manning’s n value which was determined through a calibration study. Calibration was carried out by comparing the model predicted water surface elevation in the main channels with that measured during the field trip in October 2005. The calibrated Manning’s coefficients are listed in Table 1.

Table 1. Manning’s coefficients for different zones shown in Fig.14

Zone Number	1	2	3	4	5	6	7
Manning’s n	0.035	0.06	0.15	0.035	0.035	0.035	0.06

A flow discharge of 10.67 m³/s was recorded at the USGS Gage number 14142500 during data collection and was used as the upstream boundary condition for the Sandy River. The flow discharge of the Columbia River was 3,483 m³/s, which represented the average flow release from the Bonneville Dam. It was found during the field trip that the flow was quite unsteady for the Columbia River, due mainly to the tidal influence and the

flow release from the Bonneville Dam. Releases from Bonneville Dam that day had a reported range of 3,341 to 3,737 m³/s. Discharges calculated at several Columbia River cross sections from the measured ADCP bottom tracking velocity data ranged from 2,784 to 3,560 m³/s. The stage at the exit of the Columbia River reach was based on the field measured data. The measured stage, however, was quite unsteady and two distinct stages were identified from the data set: 1.448 m and 1.676 m. Both were used for the model runs. Post-simulation analysis indicated that the difference in the stage at the exit only influenced results near the confluence area of the Sandy River and Columbia River.

The unsteady simulation started from an initial condition that assumed both rivers were dry. With a time step of 5 seconds, the steady state solution was obtained after 60,000 time steps (83 hours). The computing time was about 4.2 hours with a desktop PC equipped with a 3.2 GHz CPU.

4.3 Results and Discussion

Two runs, Run 1 and Run 2, are reported here for the calibration and validation study. The parameters of the two runs are identical except for the stage at the exit of the solution domain. Run 1 used the low measured stage (1.448 m) while Run 2 used the high stage (1.676 m). Two model runs provide information about the model sensitivity to the exit boundary condition which has a high uncertainty due to tidal influence.

The simulated water surface elevation on the Sandy River is compared with the field data in Fig.15a. It is seen that the model predicts the water elevation along the Sandy River well despite uncertainty in the measured data and the unsteady nature of the flow. The thalweg profile is also plotted in the figure to show the degree of agreement despite large fluctuations in the bed elevation. The difference between the measured and predicted elevation is less than 0.1 m except near the confluence of the west distributary and the

Columbia River. This area is influenced by the tidal fluctuation. Major elevation changes at the riffle and pool areas are captured by the model. It indicates that the bed topography represented the riffle and pool areas well and that the model represented the flow roughness correctly. Comparison of the water elevation on the Columbia River is shown in Fig.15b. When different stages were used at the exit, the model predicted the water surface elevation within the range of the measured data. Comparison of the simulated and field measured water elevations shows a satisfactory agreement along the Columbia River reach.

Validation of the model was carried out by comparing the predicted velocity with the field data. ADCP measured velocity data were collected during the project along both the Sandy and Columbia Rivers (Lai et al., 2006). The depth-averaged velocity data were processed from the ADCP velocity profiles. In both rivers, a measured data point represents an instantaneous, depth-averaged velocity for a single location. As a result, the data can be noisy. Measured and predicted velocity magnitude comparisons at all measurement points are made for both the Sandy River (Fig.16a) and the Columbia River (Fig.16b). The agreement between the model and measured data are reasonable despite the noisy measured data. Large fluctuations in the measured velocities may be partly attributed to flow unsteadiness created by local geometry features, such as boulders and large turbulent eddies, and partly due to a few erroneous field data points. More detailed velocity vector comparisons for seven segments of the two rivers were also made. They are not reported here due to space limitation, but are available in the report of Lai et al. (2006). Comparison of the predicted and measured velocity showed a reasonable agreement.

5. CONCLUDING REMARKS

An unstructured hybrid mesh numerical method is developed to solve the 2D depth-averaged flow equations. The method is applicable to arbitrarily-shaped mesh cells and offers a framework to unify many mesh topologies into a single formulation. The proposed numerical method is well suited to natural river flows with a combination of main channels, side channels, bars, floodplains and in-stream structures. The technical details of the method are presented, along with verification studies using a number of simple flow cases. The model is also applied to a natural river for practical validation study. Specific findings include the following:

(1) Different meshes have been used and demonstrated with the model, including the structured quadrilateral mesh, the unstructured triangular mesh, and the hybrid mesh. The results with different meshes compare favorably with the analytical solutions or experimental data. Triangular cell near a steep bank is less accurate than the quadrilateral cell if the total number of cells is the same. More triangular cells are needed to achieve a similar accuracy.

(2) Water surface elevation is less sensitive to the choice of meshes or even the size. However, the velocity distribution is more sensitive to the mesh. Particularly near a steep bank, more mesh cells may be needed near the bank.

(3) The parabolic turbulence model may be adequate to predict the water surface elevation or the velocity for most flow areas. However, it is less accurate for flow velocity prediction in areas of flow separation or steep banks. For flows with separation or steep banks, the $k - \varepsilon$ turbulence model is recommended.

(4) The measured water surface elevation is the recommended data for calibrating the Manning's roughness coefficient, which is the only calibration parameter recommended. It

is shown that the water surface elevation is an easier variable to model, while the velocity distribution and the associated bed shear stress need finer mesh.

6. ACKNOWLEDGEMENT

The author would like to acknowledge the peer review by Blair Greimann and Rob Hilldale at the Technical Service Center of the Bureau of Reclamation. The work was partially supported by the Bureau of Reclamation Science and Technology Program under project number 0092.

7. REFERENCES

- Baker, T. J. (1996). "Discretization of Navier–Stokes equations and mesh-induced errors." *Proc., 5th Int. Conf. Numerical Grid Generation in Computational Field Simulation*, Mississippi State Univ., Mississippi.
- Begnudelli, L., and Sanders, B.F. (2006). "Unstructured grid finite-volume algorithm for shallow-water flow and scalar transport with wetting and drying." *J. Hydraulic Engr., ASCE*, 132(4), 371-484.
- Bernard, R. S., and Berger, R. C. (1999). "A parallel coupling scheme for disparate flow solvers." Department of Defense High Performance Computing Modernization Program, 1999 Users Group Conference, June 1–10, Monterey, Calif.
- Brunner, G.W., (2006). "HEC-RAS, River Analysis System User's Manual - version 4.0," US Army Corps of Engineers, Hydrologic Engineer Center, Davis, California.
- Chow, V.T., and Ben-Zvi, A. (1973). "Hydrodynamic modeling of two-dimensional watershed flow." *J. Hydraul. Div., ASCE*, 99(11), 2023-2040.

- DHI (1996). "MIKE21 hydrodynamic module users guide and reference manual," Danish Hydraulic Institute - USA, Eight Neshaminy Interplex, Suite 219, Trevoise, PA.
- DHI (2002). "MIKE11, A modelling system for rivers and channels, Reference manual," DHI Water & Environment, Hørsholm, Denmark.
- Ghamry, H.K., and Steffler, P.M. (2005). "Two dimensional depth-averaged modeling of flow in curved open channels." *J. Hydraulic Res., IAHR*, 43(1), 44–55.
- Harrington, R.A., Kouwen, N., and Farquhar, G.J. (1978). "Behavior of hydrodynamic finite element model." *Finite Elements in Water Resources. Proc. 2nd Int. Conf. on Finite Elements in Water Resources*, Imperial College, London, pp. 2.43–2.60.
- Hervouet, J.M., and van Haren, L. (1996). "Recent advances in numerical methods for fluid flow." in Anderson, M.G., Walling, D.E. and Bates, P.D. (editors), *Floodplain Processes*, John Wiley, Chichester.
- Huang, J.V., and Greimann, B. P. (2007). "User's manual for SRH-1D V2.0," Sedimentation and River Hydraulics Group, Technical Service Center, Bureau of Reclamation, Denver, CO 80225. website: www.usbr.gov/pmts/sediment/
- Jia, Y., and Wang, S.S.Y. (2001). "CCHE2D: two-dimensional hydrodynamic and sediment transport model for unsteady open channel flows over loose bed." Technical Report No. NCCHE-TR-2001-1, School of Engineering, The University of Mississippi, University, MS 38677.
- Jin, Y.C., and Steffler, P.M. (1993). "Predicting flow in curved open channel by depth-averaged method." *J. Hydraulic Eng., ASCE*, 119(1), 109–124.
- Kramer, T., and Jozsa, J. (2007). "Solution-adaptivity in modelling complex flows." *Computers & Fluids*, 36(3), 562-577.

- Lai, Y.G., So, R.M.C., and Przekwas, A.J. (1995). "Turbulent transonic flow simulation using a pressure-based method," *Int. J. Engineering Sciences*, 33(4), 469-483.
- Lai, Y.G. (2000). "Unstructured grid arbitrarily shaped element method for fluid flow simulation," *AIAA Journal*, 38 (12), 2246-2252.
- Lai, Y.G., Weber, L.J., and Patel, V.C. (2003). "Non-hydrostatic three-dimensional method for hydraulic flow simulation - Part I: formulation and verification," *J. Hydraul. Eng., ASCE*, 129(3), 196-205.
- Lai, Y.G. (2006). *Theory and User Manual for SRH-W, version 1.1*, Sedimentation and River Hydraulics Group, Technical Service Center, Bureau of Reclamation, Denver, CO 80225. website: www.usbr.gov/pmts/sediment/
- Lai, Y.G., Holburn, E.R., and Bauer, T.R. (2006). "Analysis of sediment transport following removal of the Sandy River Delta Dam," Project Report, Sedimentation and River Hydraulics Group, Technical Service Center, Bureau of Reclamation, Denver, CO.
- Leopold, L.B., and Wolman, M.G. (1960). "River meanders." *Geol. Soc. Ann. Bull.*, 71, 769-793.
- MacDonald, I. (1996). "Analysis and computation of steady open channel flow," Ph.D. Thesis, Dept. of Mathematics, Univ. of Reading, U.K.
- McGuirk, J.J., and Rodi, W. (1978). "A depth averaged mathematical model for near field of side discharge into open channel flow." *J. Fluid Mech.*, 86(4), 761-781.
- Patankar, S.V. (1980). *Numerical Heat Transfer and Fluid Flow*, McGraw-Hill, New York.
- Peric, M., Kessler, R., and Scheuerer, G. (1988). "Comparison of finite volume numerical methods with staggered and collocated grids." *Computers in Fluids*, 16(4), 389-403.

- Rhie, C.M., and Chow, W.L. (1983). "Numerical study of the turbulent flow past an airfoil with trailing edge separation," *AIAA Journal*, 21(11), 1526-1532.
- Rodi, W. (1993) "Turbulence models and their application in hydraulics," 3rd Ed., IAHR Monograph, Balkema, Rotterdam, The Netherlands.
- Shettar, A.S., and Murthy, K.K. (1996). "A numerical study of division of flow in open channels." *J. Hydraulic Research, IAHR*, 34(5), 651-675.
- Schumm, S.S. (1960). "The shape of alluvial channel in relation to sediment type." USGS Professional Paper, 352-B.
- USACE, US Army Corps of Engineers, (1996). "Users guide to RMA2 - version 4.3," US Army Corps of Engineers, Waterway Experiment Station - Hydraulic laboratory, Vicksburg, MS.
- Vreugdenhil, C.B, and Wijnbenga, J. (1982). "Computation of flow pattern in rivers." *J. Hydraul. Div., ASCE*, 108(11), 1296-1310.
- Wu, W. and D.A. Vieira, (2002) "One-dimensional channel network model CCHE1D version 3.0 – technical manual," *Technical Report No. NCCHE-TR-2002-1*, National Center for Computational Hydroscience and Engineering, The University of Mississippi, Oxford, MS.
- Ye, J., and McCorquodale, J.A. (1997). "Depth averaged hydrodynamic model in curvilinear collocated grid." *J. Hydraul. Eng., ASCE*, 123(5), 380-388.

Zarrati, A.R., Tamai, N., and Jin, Y.C. (2005). "Mathematical modeling of meandering channels with a generalized depth averaged model." *J. Hydraul. Eng., ASCE*, 131(6), 467-475.

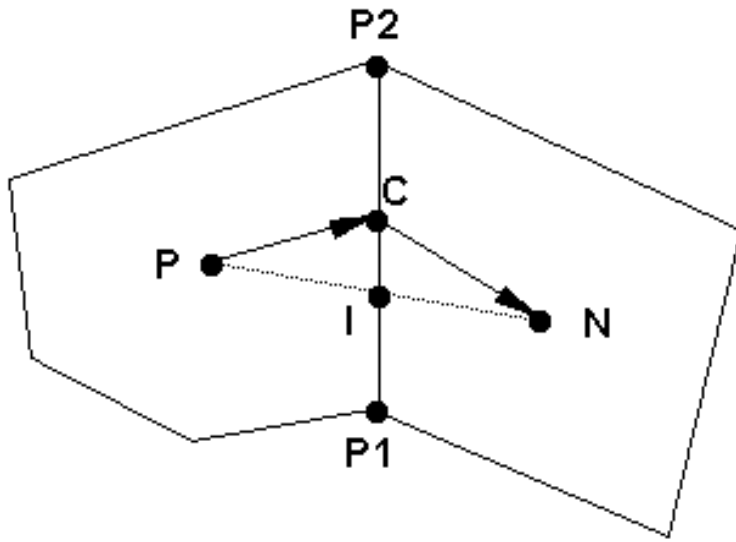


Figure 1. Schematic illustrating a polygon cell P along with one of its neighboring polygons N

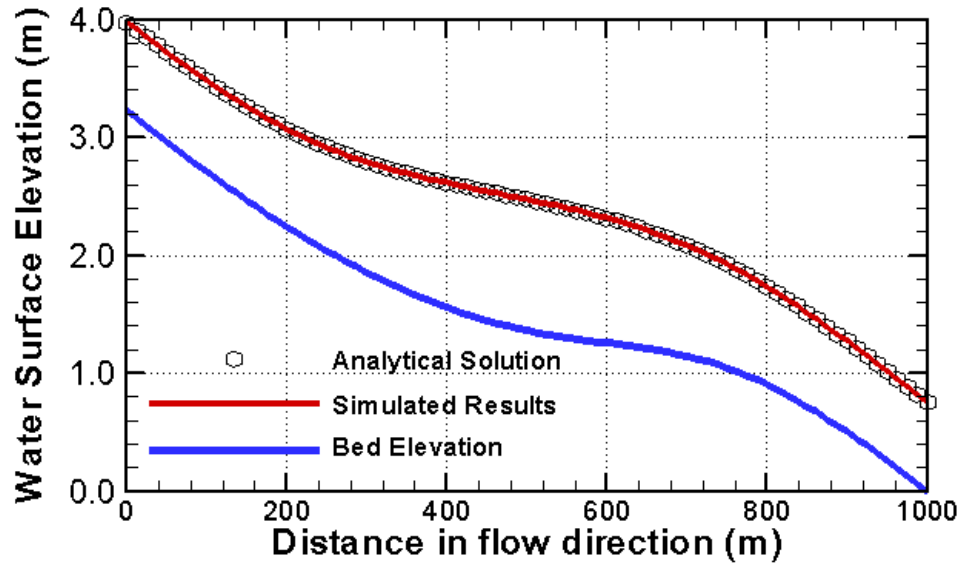


Figure 2. Comparison of simulated water surface elevation with analytical solutions for Case 1 of MacDonald (1996).

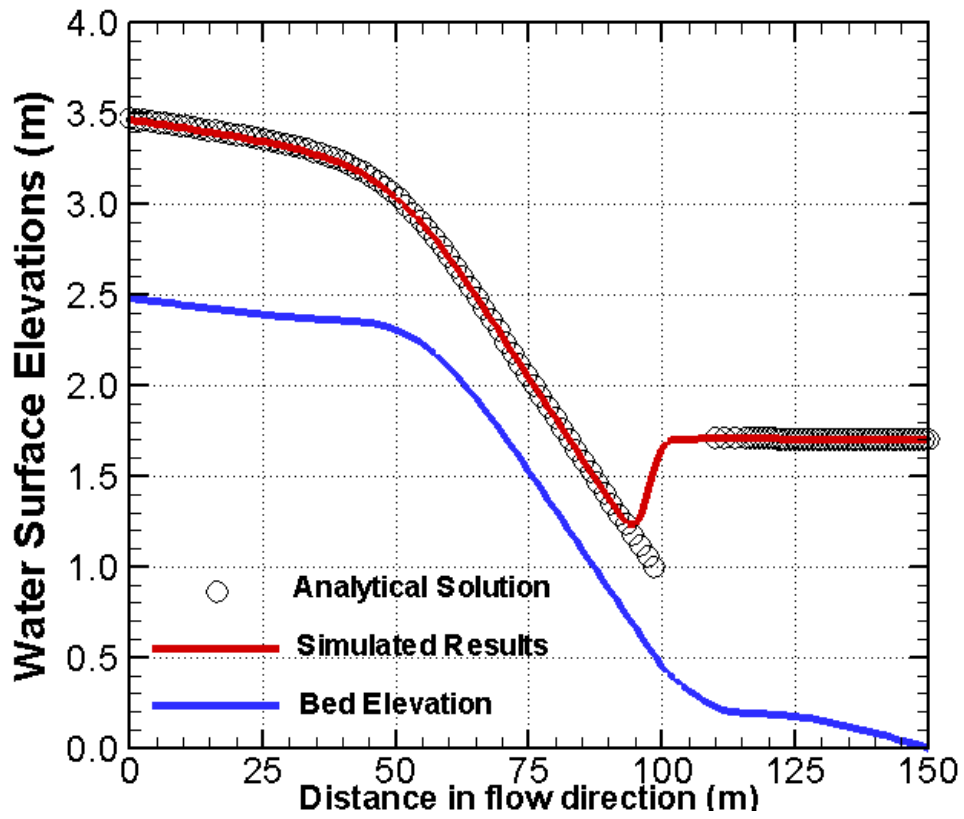


Figure 3. Comparison of simulated water surface elevation with analytical solutions for Case 6 of MacDonald (1996).

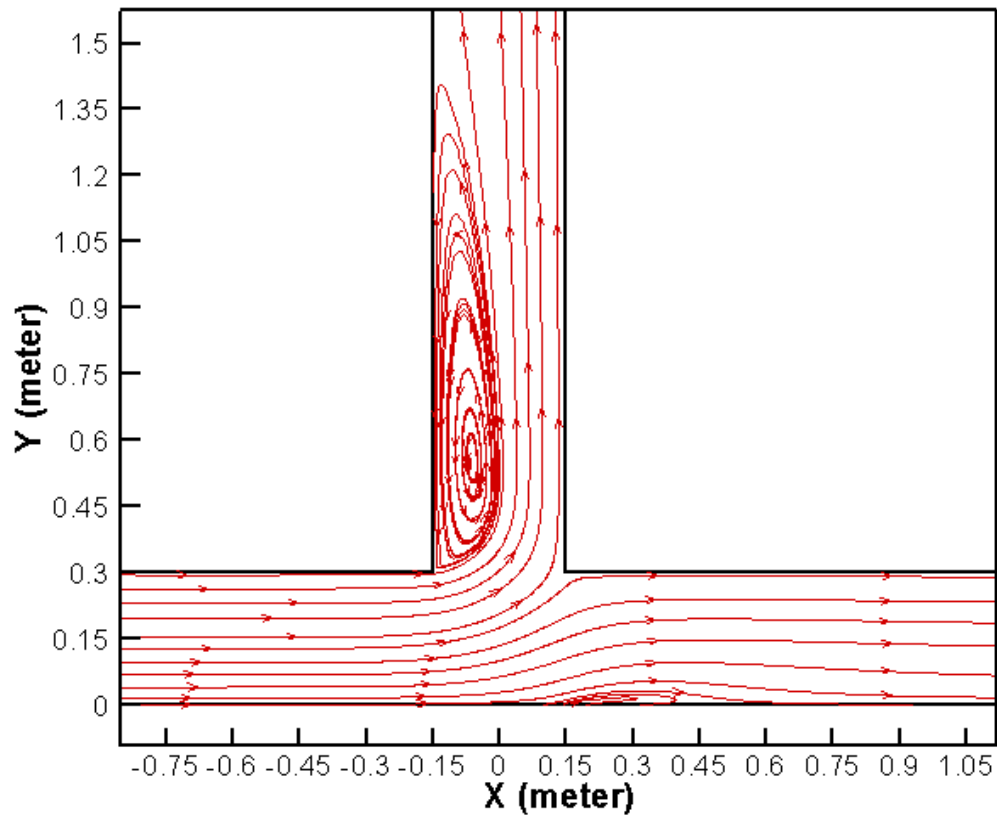
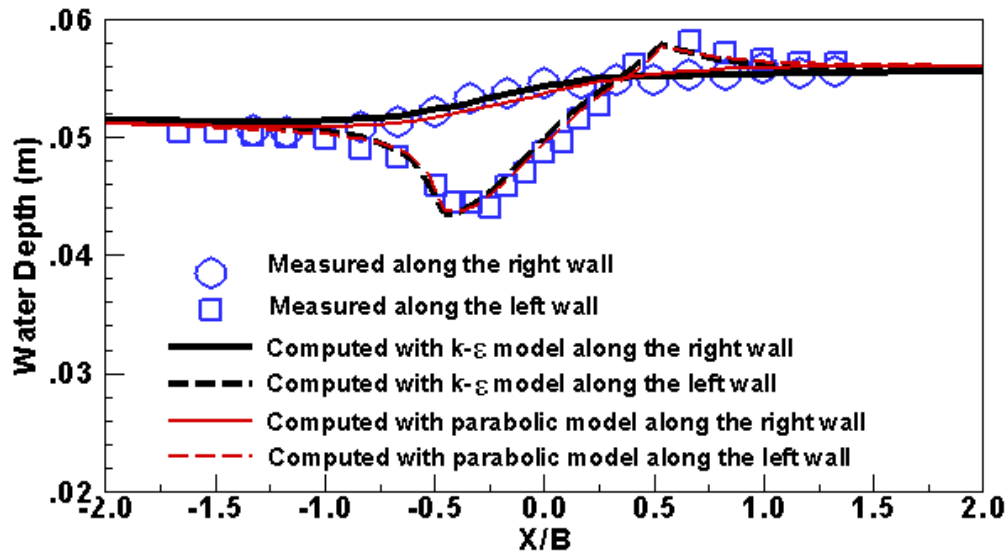
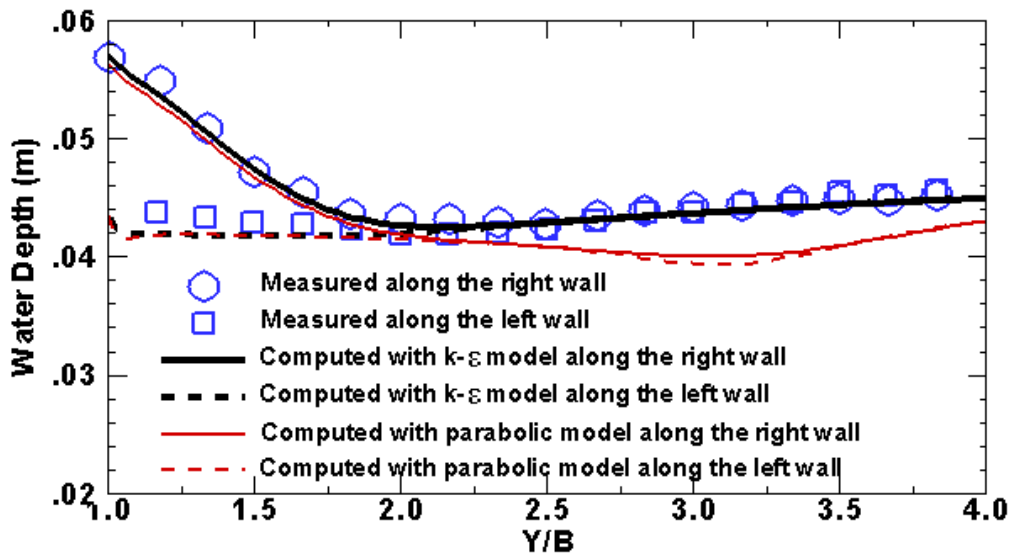


Figure 4. Layout of the solution domain and the predicted flow pattern with the $k - \varepsilon$ model for the case of Shettar and Murthy (1996).



(a) Along the main channel



(b) Along the side channel

Figure 5. Comparison of water depth along both walls of the main and side channels for the case of Shettar and Murthy (1996). Left and right are defined when facing the main flow direction of the channel.

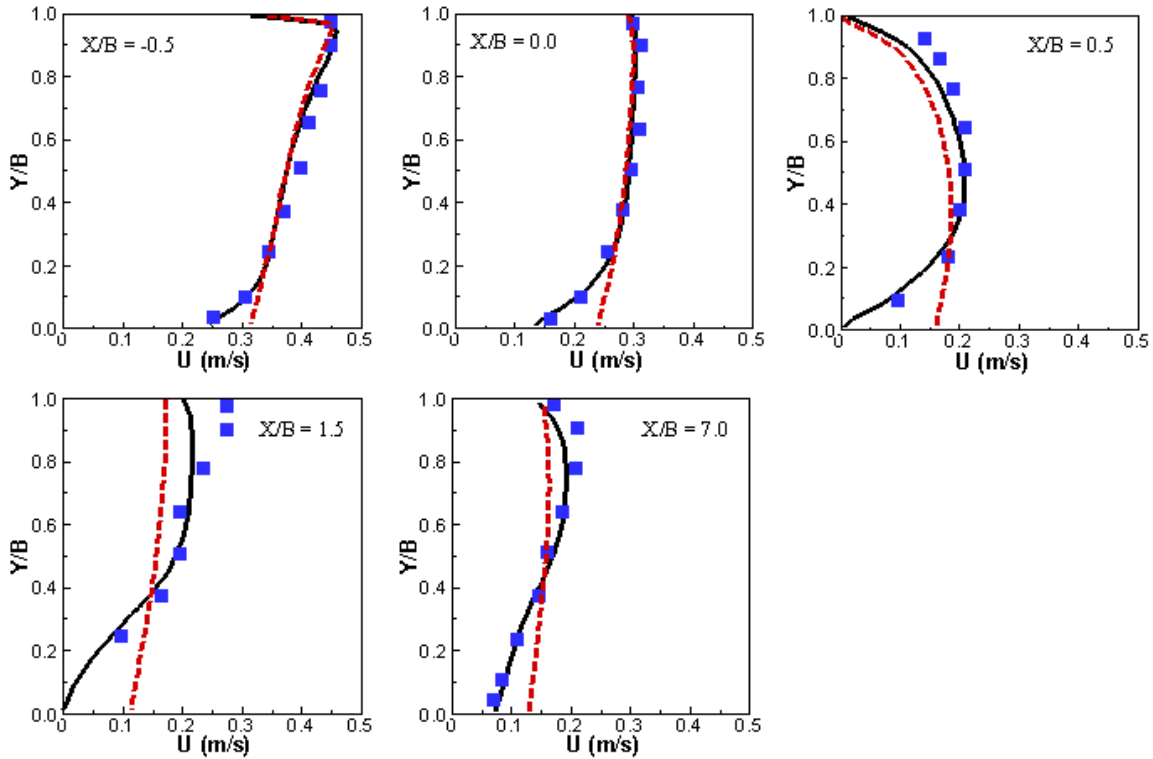


Figure 6. Comparison of x-velocity profiles at selected x locations in the main channel for the case of Shettar and Murthy (1996). Symbols: measured data; Solid lines: computed results with the $k - \varepsilon$ model; Dashed lines: computed results with the parabolic model.

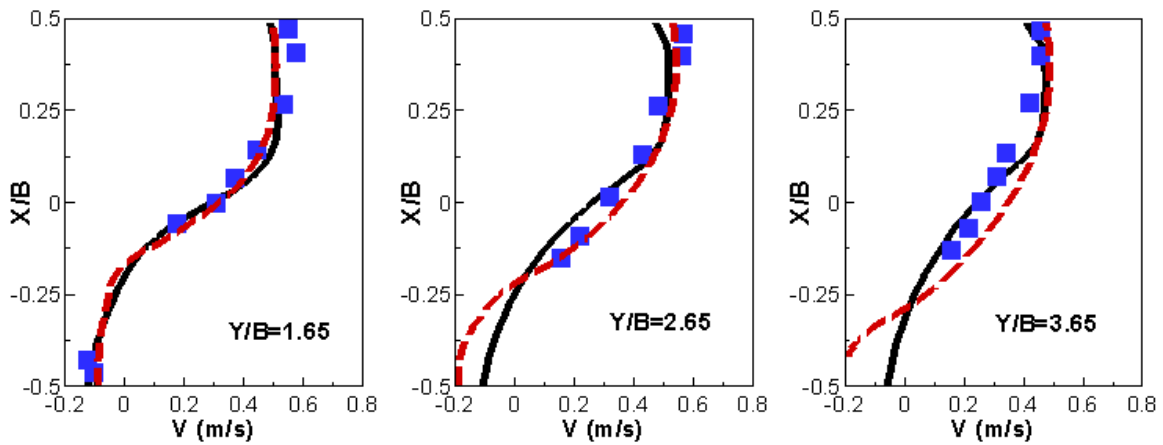


Figure 7. Comparison of y-velocity profiles at selected y locations in the side channel for the case of Shettar and Murthy (1996). Symbols: measured data; Solid lines: computed results with the $k - \varepsilon$ model; Dashed lines: computed results with the parabolic model.

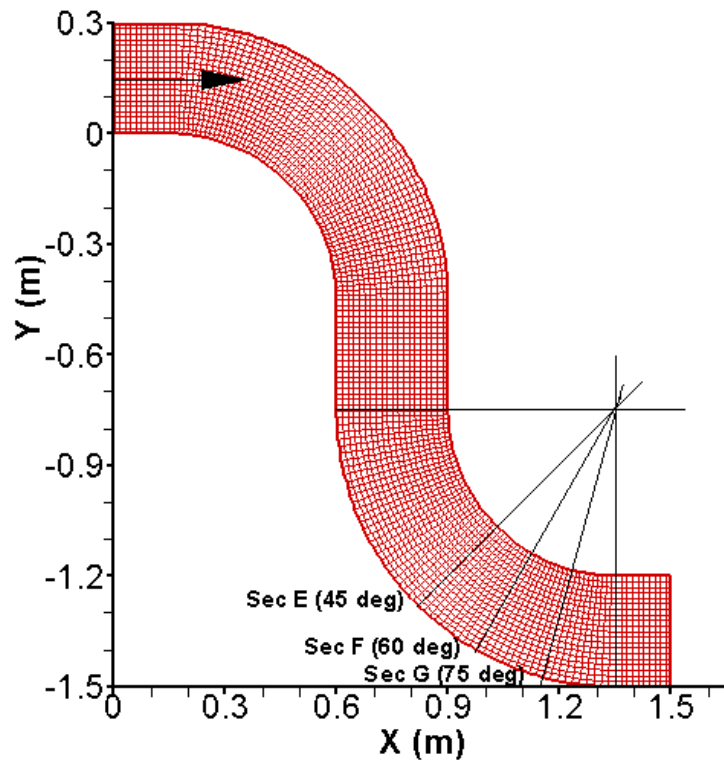
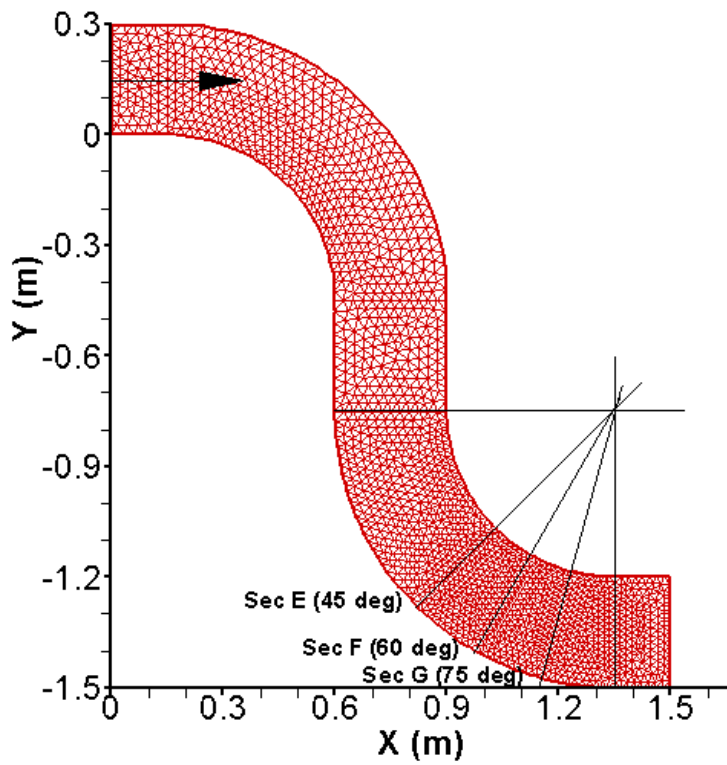
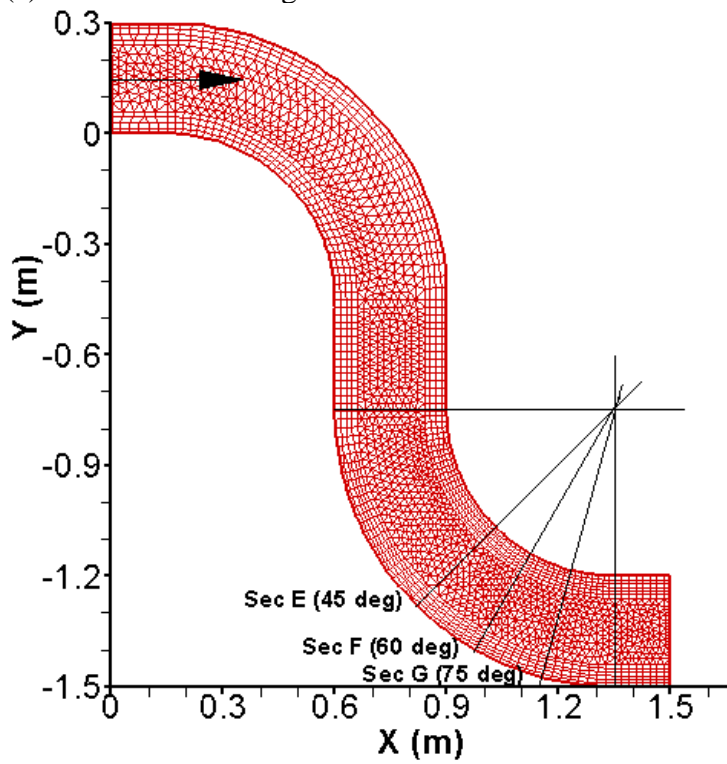


Figure 8. The geometry and the structured quadrilateral mesh of the meandering channel



(a) Unstructured triangular mesh



(b) Hybrid quadrilateral and triangular mesh

Figure 9. The unstructured triangular mesh and the hybrid mesh used for the meandering channel simulation.

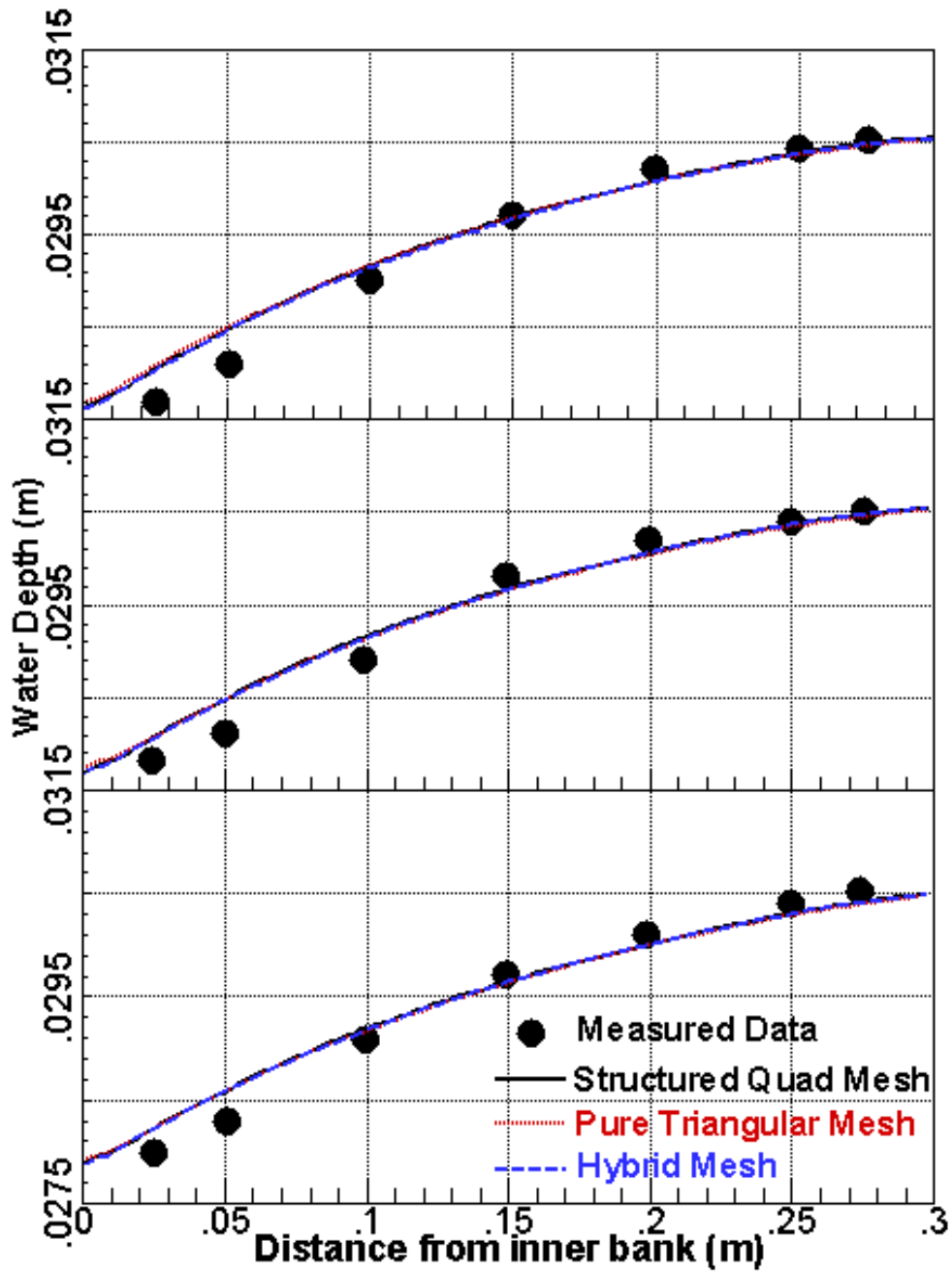


Figure 10. Comparison of lateral water surface elevation distributions at three cross sections for three meshes.

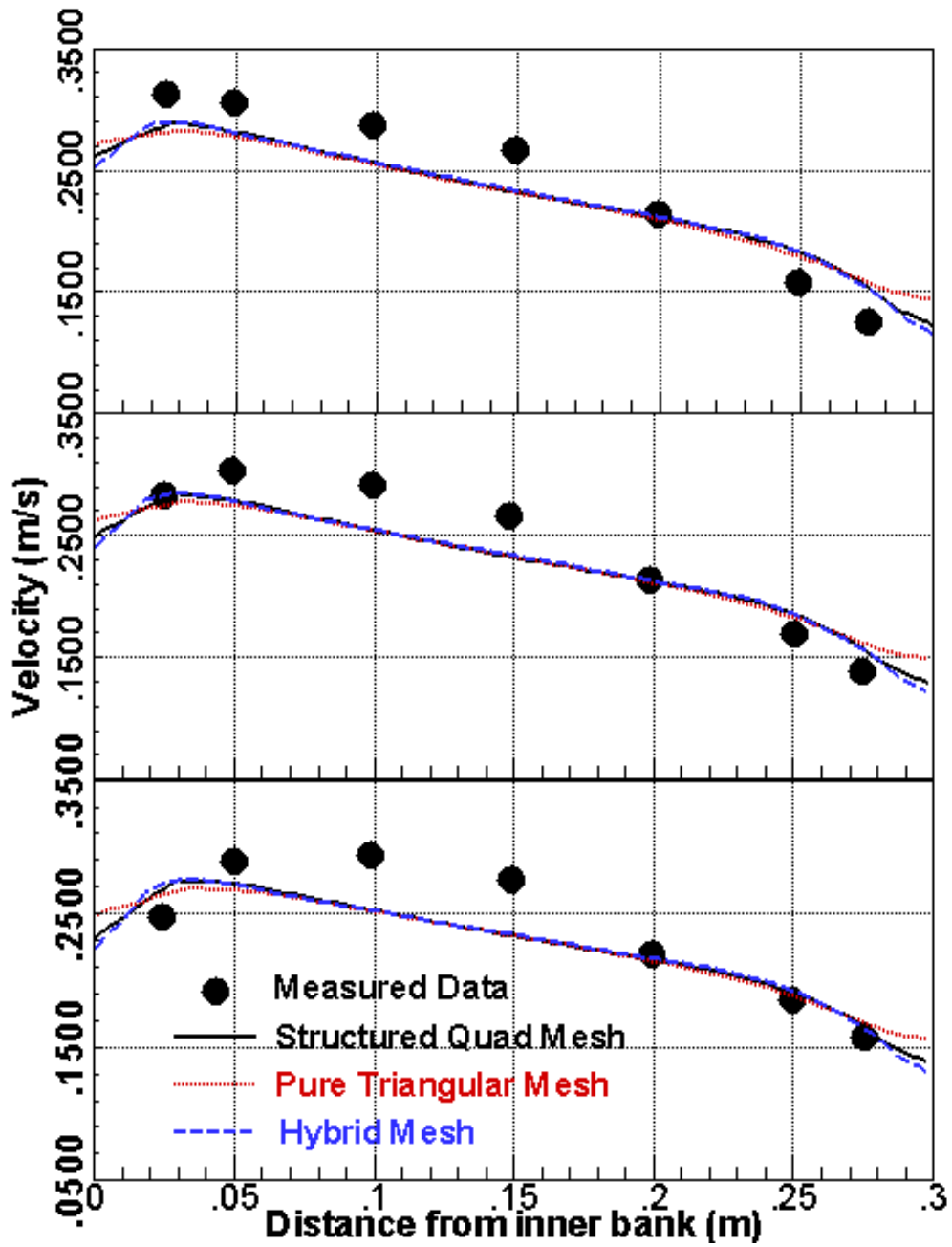


Figure 11. Comparison of lateral velocity distributions at three cross sections for three meshes.

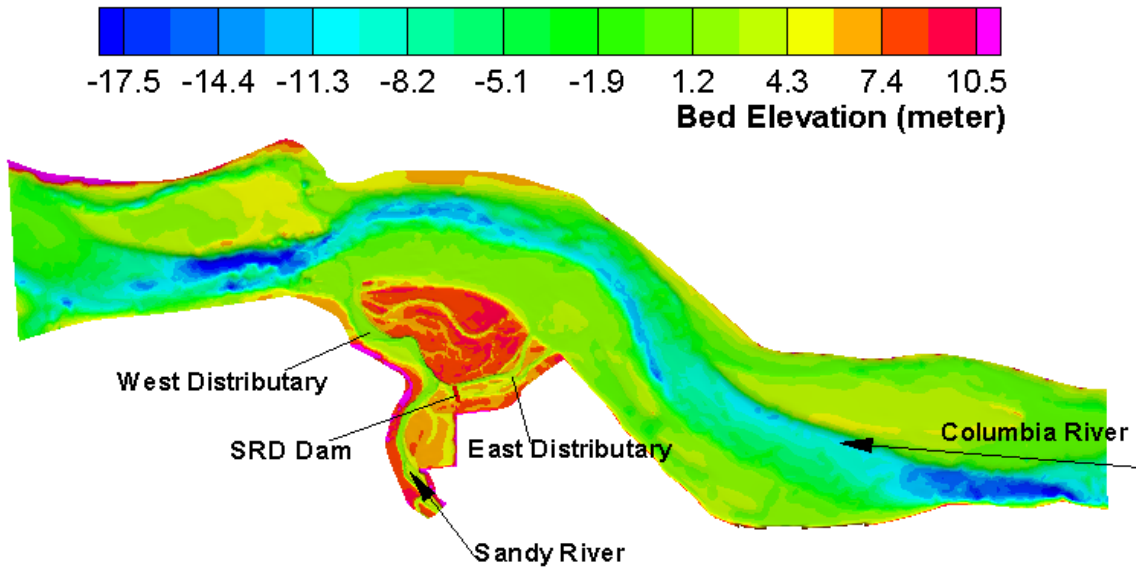


Figure 12. The study area of the Sandy and Columbia River confluence, along with the topography for the solution domain.

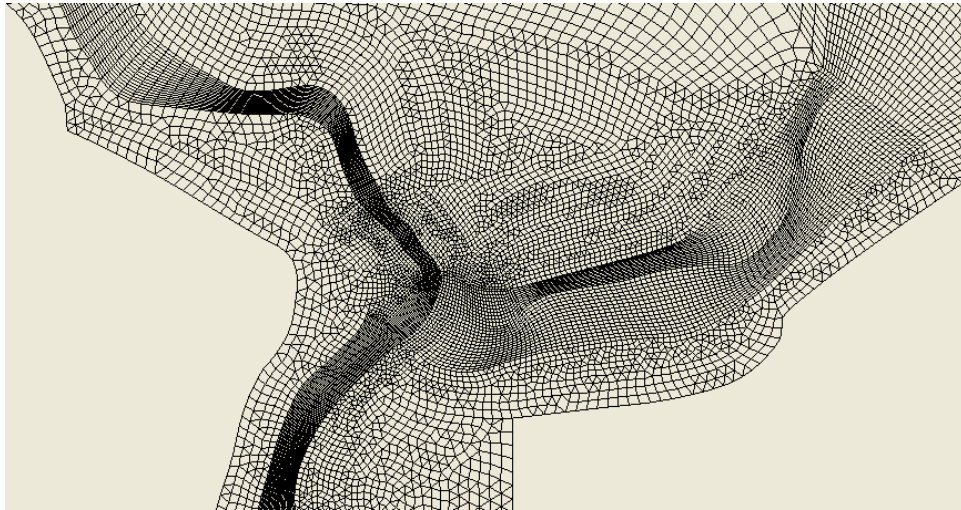


Figure 13. A portion of the mesh used to model the Sandy River and Columbia River Delta

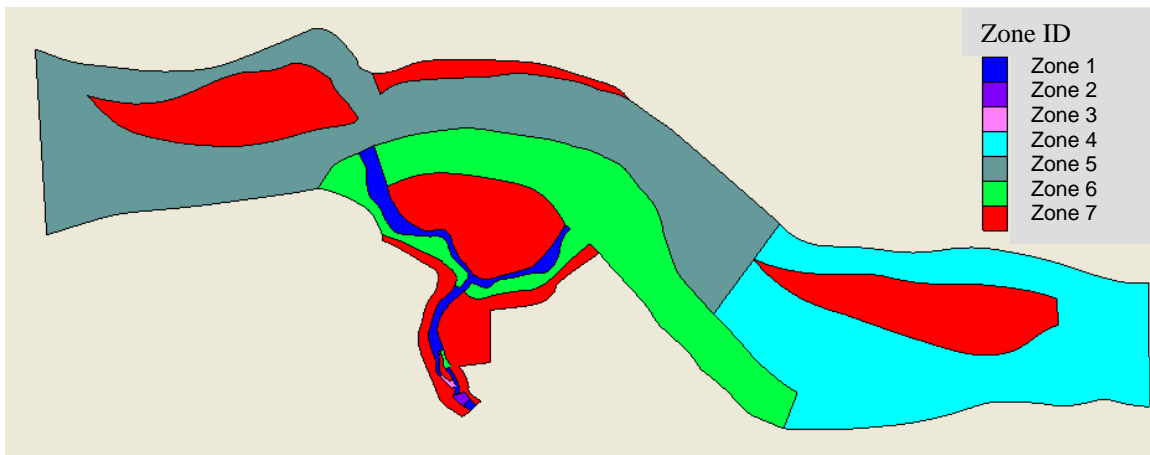
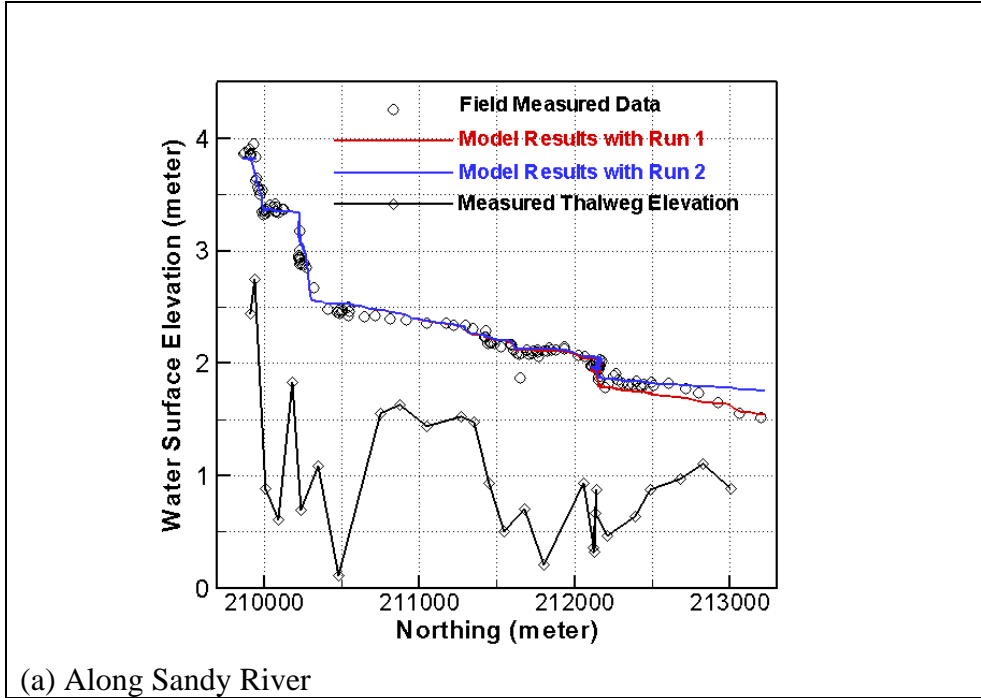
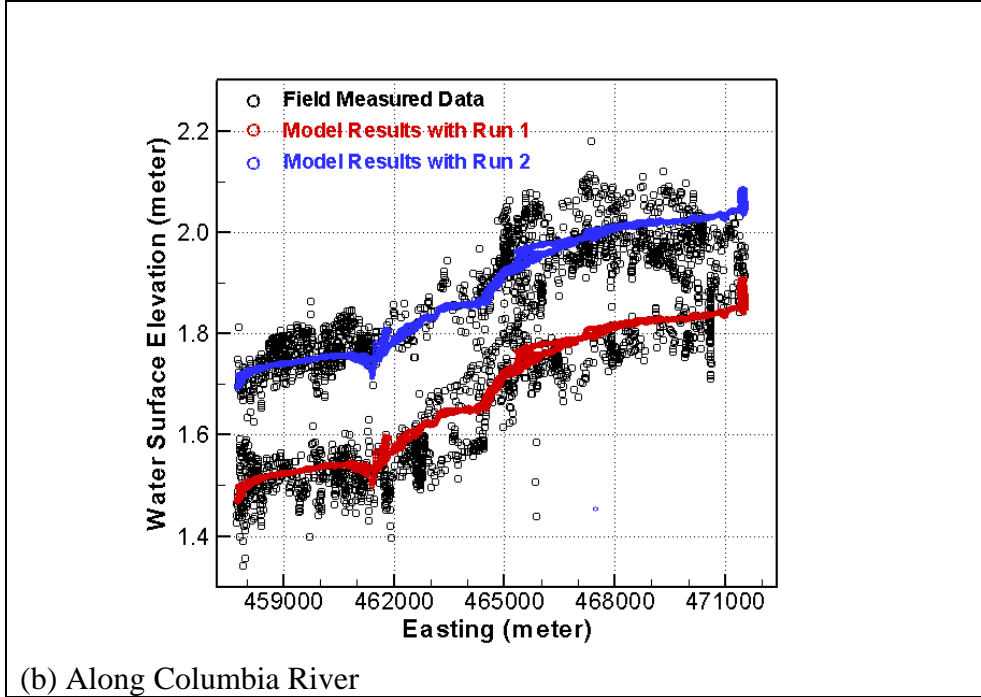


Figure 14. Roughness zones used for the Sandy River Delta simulation

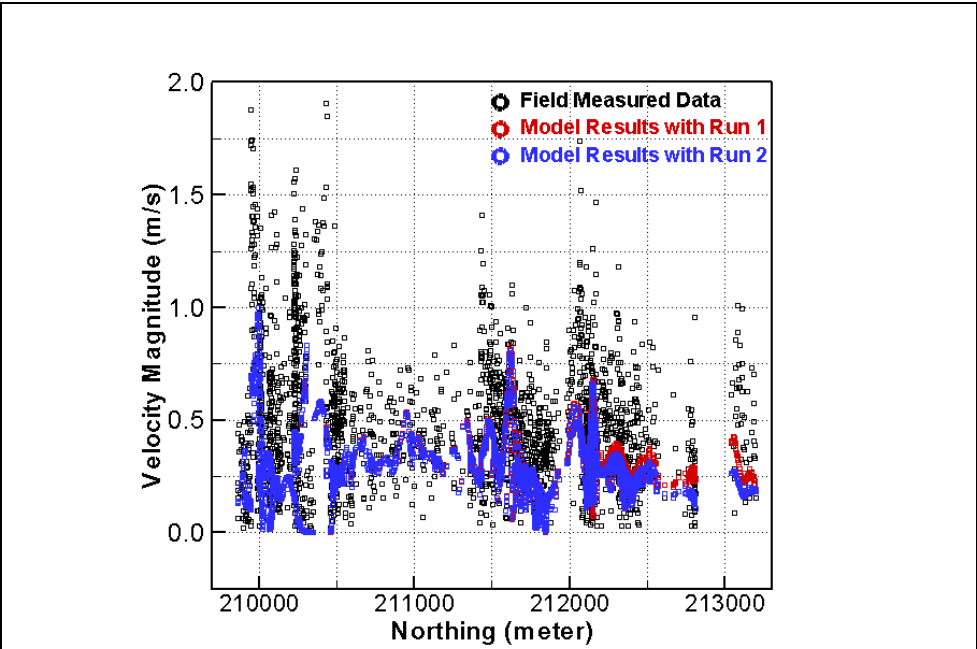


(a) Along Sandy River

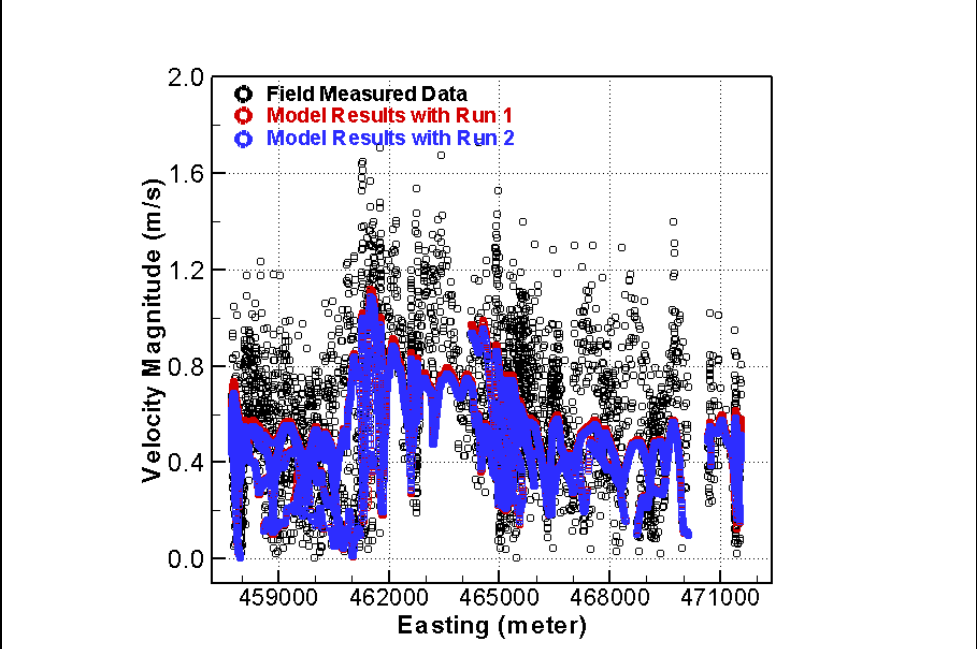


(b) Along Columbia River

Figure 15. Comparison of field measured and model predicted water surface elevations for the October 12, 2005 flow conditions



(a) Along Sandy River



(b) Along Columbia River

Figure 16. Comparison of field measured and model predicted depth-averaged velocity for the October 12, 2005 flow conditions